Chemical Geology 533 (2020) 119431

Contents lists available at ScienceDirect

Chemical Geology

journal homepage: www.elsevier.com/locate/chemgeo

# Microscale trace-element distribution across the Cretaceous/Palaeogene ejecta layer at the Agost section: Constraining the recovery of pre-impact conditions

Claudia Sosa-Montes de Oca[a,*], Gert J. de Lange[b], Francisca Martínez-Ruiz[c], Miguel Ortega-Huertas[d], Francisco J. Rodríguez-Tovar[a]

[a] Departamento de Estratigrafía y Paleontología, Universidad de Granada, Avda. Fuentenueva s/n, 18002 Granada, Spain
[b] Department of Earth Sciences—Geochemistry, Utrecht University, 3584 CD Utrecht, the Netherlands
[c] Instituto Andaluz de Ciencias de la Tierra, IACT, CSIC-Universidad de Granada, Avda. Las Palmeras 4, 18100 Armilla, Granada, Spain
[d] Departamento de Mineralogía y Petrología, Universidad de Granada, Avda. Fuentenueva s/n, 112002 Granada, Spain

ARTICLE INFO

Editor: Dr. Don Porcelli

*Keywords:*
KPgB
Ejecta layer
LA-ICP-MS
Palaeoenvironmental reconstruction
Microscale analyses

ABSTRACT

A high-resolution, sub-mm scale analysis of the distribution of major and trace elements across the ejecta layer marking the Cretaceous/Palaeogene boundary (KPgB) at the Agost section (SE Spain) was performed using Laser Ablation-Inductivity Coupled Plasma-Mass Spectrometry (LA-ICP-MS). A KPgB interval ≈17 mm thick, has been selected for this study. It includes gray calcareous marl from the uppermost Maastrichtian (Cretaceous), 2.02-mm-thick red clay (the ejecta layer), and blackish-gray clay (boundary clay layer) from the lowermost Danian (Palaeogene). The unconsolidated sediments were resin-embedded under $O_2$-free conditions and analyzed by LA-ICP-MS line continuous scan measurements at 20 μm increments and a laser-beam of 120 μm. These micron-scale analyses show that the anomalous contents of trace and major elements in this boundary are restricted to the ejecta layer, which displays a relatively uniform distribution over its ≈2 mm thickness. Trace and major elemental ratios, such as Ca/Al, Ti/Al, Cr/Al, Fe/Al, Ni/Al, Cu/Al, Zn/Al, As/Al, Sb/Al and Pb/Al have similar values below and above the ejecta layer, consistent with similar palaeoenvironmental conditions prior to and after the impact event. Such element distribution points to anomalies exclusively restricted to the ejecta, thus a nearly instantaneous re-establishment of pre-impact conditions right after the impact event is observed.

## 1. Introduction

The link between the major mass extinction at the end of the Cretaceous (KPgB), i.e. 66.04 Ma (Husson et al., 2014; Schulte et al., 2010a), and the Chicxulub asteroid impact event, has been broadly demonstrated (Renne et al., 2013). This impact entailed important short and long-term palaeoenvironmental changes worldwide (Kring, 2007; Vellekoop et al., 2018), including the instantaneous input of $CO_2$ into the atmosphere-ocean system (Artemieva and Morgan, 2017) analogous to current anthropogenic $CO_2$ input (Pachauri et al., 2014). Currently, the relationship between the KPg mass extinction and a meteorite impact is widely accepted however, alternative or complementary mechanisms, especially volcanism associated with the Deccan Traps, are still considered (Renne et al., 2015; Schoene et al., 2015, 2019). Although this event has been profusely studied, there are still debated issues such as the re-establishment time of pre-impact conditions or the recovery of biological productivity after this mass extinction (e.g., Lowery et al., 2018). To assess these aspects it is fundamental to understand the evolution of environmental conditions prior to, during, and after the impact event.

Major geochemical anomalies, recognized worldwide, characterize this boundary in both marine and continental depositional environments (Goderis et al., 2013). However, the extraterrestrial contribution is particularly evident in the ejecta layer of marine distal sites, those located more than 5000 km from the Chicxulub impact crater (Claeys et al., 2002; Goderis et al., 2013; Smit, 1999; Urrutia-Fucugauchi and Pérez-Cruz, 2016). The Agost (SE Spain) section is one of the best exposed and most representative of marine distal areas for the KPgB event (Molina et al., 2005; Rodríguez-Tovar et al., 2006). This section has been intensely studied, thus an adequate background information is

* Corresponding author.
*E-mail addresses:* csosa@ugr.es, csm@csic.es (C. Sosa-Montes de Oca), G.J.deLange@uu.nl (G.J. de Lange), fmruiz@ugr.es, fmruiz@iact.ugr-csic.es (F. Martínez-Ruiz), fjrtovar@ugr.es (F.J. Rodríguez-Tovar).

https://doi.org/10.1016/j.chemgeo.2019.119431
Received 19 March 2019; Received in revised form 20 November 2019; Accepted 27 November 2019
Available online 14 December 2019

available for our high-resolution approach.

The distribution of trace elements is crucial for the reconstruction of the palaeoenvironmental parameters associated with the impact (e.g., Goderis et al., 2013; Smit and Ten Kate, 1982), and to evaluate oxygenation conditions. However, appropriate high-resolution sampling across the KPgB is a challenge, due to the different lithologies of the transition and the millimetric to few centimeters scale thickness of the ejecta and boundary clay layers.

Sosa-Montes de Oca et al. (2018a, 2018b) have explored a novel methodology in the KPgB sediments at the Agost section, enabling high-resolution LA-ICP-MS analyses in continuous mode after resin embedding. In these contributions, the high potential of the methodology was demonstrated. In this study we have used this novel methodology though applied to the high-resolution analysis of the ejecta layer that has not been previously studied by using this method since preservation in the formerly studied section was not good enough.

Hence we have used intact segments of the KPgB at Agost and LA-ICP-MS in continuous high-resolution laser mode (μm-scale) after resin embedding, to obtain a high-resolution profiles of elemental ratios, Ca/Al, Ti/Al, Cr/Al, Fe/Al, Cu/Al, Ni/Al, Zn/Al, As/Al, Sb/Al and Pb/Al, across the ≈2 mm thick ejecta layer, in order to provide new insights into the duration of environmental perturbations derived from the impact event.

## 2. Geological setting

The KPgB distal section of Agost (38°27′3.31″N; 0°38′9.71″E) is located at km 9 on the west side of road CV-827, north of the town of Agost, Alicante (Southeast Spain) (Fig. 1). At the time of the KPgB impact, the Agost site was located offshore, in a upper-bathyal setting (~600 to 1000 m depth) (Schulte et al., 2010b), at around 27–30° N palaeolatitude (Smith et al., 1981). Lithologically, the Agost section comprises (Fig. 1): (a) Cretaceous sediments consisting of gray calcareous marl and marl of Late Maastrichtian age (uppermost Cretaceous), overlain by lowermost Palaeogene sediments (Early Danian), including (b) 2.02-mm-thick of a red clay ejecta layer, and (c) a blackish-gray boundary clay interval (see a, b and c in Fig. 1). The ejecta layer, at the distal sections, marks the sharp contact between the Maastrichtian and Danian, and is known to contain impact evidence such as spherules (Glass and Burns, 1987; Martínez-Ruiz et al., 1997; Smit, 1990, 1999; Smit and Klaver, 1981), iridium and other platinum-group element (PGE) anomalies (Alvarez et al., 1980, 1990; Claeys et al., 2002; Smit and Ten Kate, 1982) as well as enhanced concentrations of Cr, Fe, Ni, and Ti which came from the meteorite, a sulphide-rich carbonaceous chondrite (Kyte, 1998; Martínez-Ruiz et al., 1997; Shukolyukov and Lugmair, 2004) and also a significant decrease of calcium carbonate (Goderis et al., 2013; Schulte et al., 2010b), a result to the mass extinction caused.

This study focuses on a ≈ 17 mm-thick interval, containing all above-mentioned facies (a, b and c; Fig. 1). According to the sedimentation rates of 2.05 cm $kyr^{-1}$ estimated for the uppermost Maastrichtian sediments (Thibault and Husson, 2016), and that of 0.83 cm $kyr^{-1}$ calculated for the lowermost Danian sediments (Groot et al., 1989), the studied material is considered to span a time interval ranging from 240 years before to 1300 years after the KPgB. Furthermore, it is thought that the ejecta layer deposition itself was a snapshot on a geological time scale, potentially in the order of days to months (Artemieva and Morgan, 2009).

## 3. Material and methods

### 3.1. Resin embedding Cretaceous-Palaeogene interval

In the studied KPgB interval of the Agost section, seven segments ~25 mm-thick were collected, all including a well-preserved visible ejecta layer. All segments were vertically sawn in two parts; one part was reserved for conventional ICP-OES and ICP-MS analyses, while in the other part resin embedding treatments were conducted (Fig. 2).

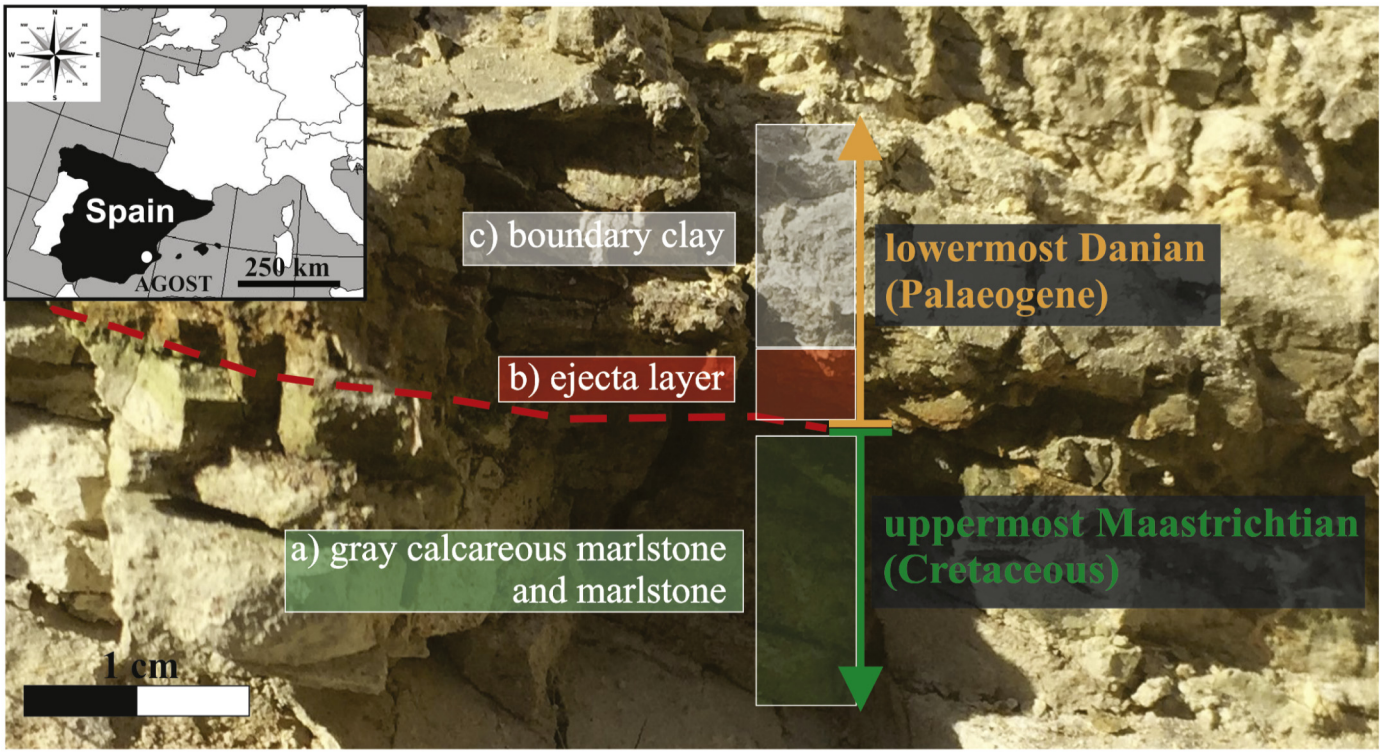


**Fig. 1.** Agost outcrop. Location of the Cretaceous-Palaeogene section (KPg) in the Agost section (Alicante, Southeast Spain). The studied Agost transition (KPgT) comprises: (a) gray calcareous marlstones and marlstones from the uppermost Maastrichtian (Cretaceous), (b) 2–3-mm-thick ejecta layer, and (c) blackish-gray boundary clay layer from the lowermost Danian (Maastrictian).

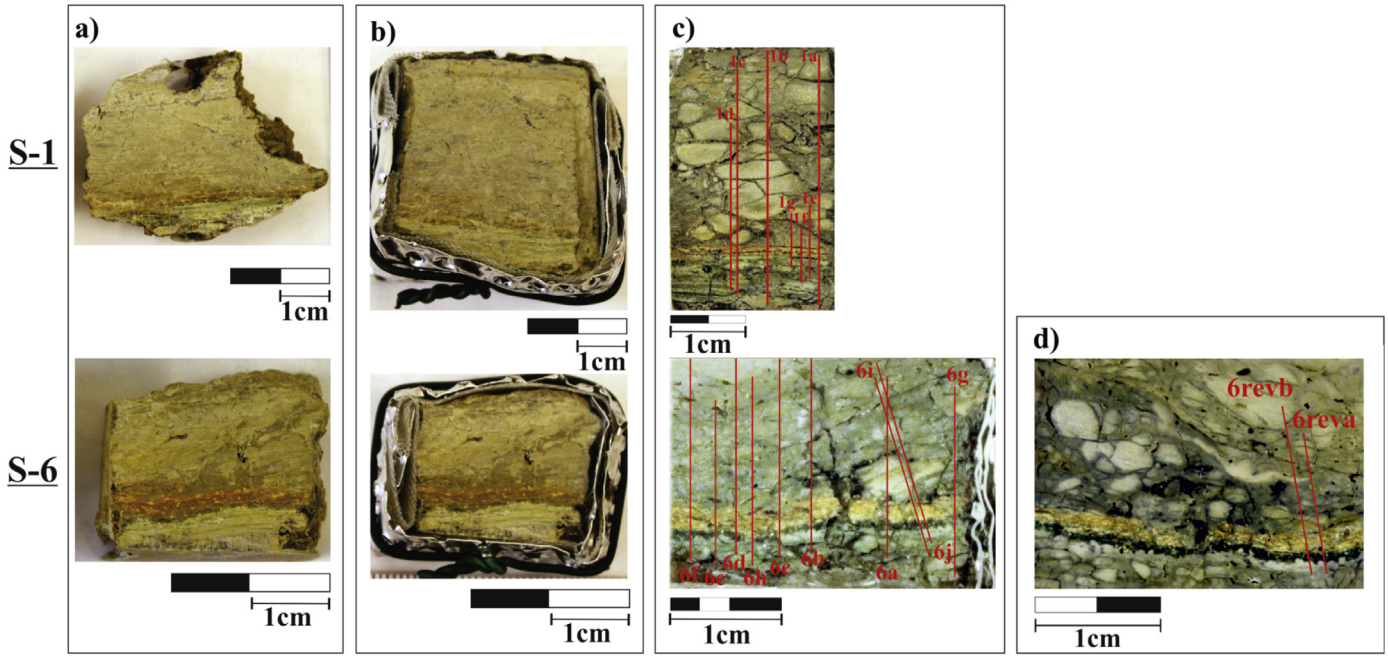


**Fig. 2.** Evolution of segments 1 and 6 (S-1 and S-6) during the resin embedding process: (a) section prior to embedding; (b) section prepared for embedding; (c) section after cutting (*) and polishing. LA-paths in red lines; (d) Black part of segment-6. (*): after embedding, the ~2 mm-thick sections were cut so as to have a clean, flat surface and being ~10 mm-thick. (For interpretation of the references to color in this figure legend, the reader is referred to the web version of this article.)

Prior to the resin embedding, the segments were reinforced, using aluminum foil (0.2 mm thickness) and Teflon mesh. To do so, we first cut the section edges as flat as possible and covered their bottom with Teflon mesh and perforated aluminum foil, fixing both with wire (Fig. 2a and b).

For resin embedding we used Spurr Epoxy Resin following the methodology specified in Hennekam et al. (2015) and Jilbert et al. (2008). The required duration of resin embedding steps depends on the dimensions of the segment. In this case, all steps were done during 26 days in an argon-filled glove box. The specific process is as follows: a) firstly, samples are treated with acetone during four consecutive days; for this, 1 l of oxygen-free acetone was used, changing every 24 h and keeping the samples always submerged, b) secondly, samples are treated with spurr epoxy resin during 22 days, in which four sub-steps were differentiated: sub-step 1: using a mixture of acetone and resin 3:1 (75% acetone: 25% resin) during four days, sub-step 2: using a mixture of acetone and resin 2:1 (66% acetone: 33% resin) during four days, sub-step 3: using a mixture of acetone and resin 1:1 (50% acetone: 50% resin) during four days, and sub-step 4: using pure spurr epoxy resin during 10 days. All exchanges were done using syringes with the different intervals remaining undisturbed inside the bath, and all handling was done inside the anoxic glove box.

After that, the different treated segments were removed from the glove box and put into the oven for curing during 48 h at 60 °C. The solid resin KPgB segments (seven segments in total) were then cut perpendicular to the bedding plane. Segments surfaces were polished and the two best segments (segments 1 and 6), in which the ejecta layer seems visibly best preserved, were analyzed by LA-ICP-MS line-scan (Fig. 2c and Fig. 2d).

### 3.2. LA-ICP-MS measurements and processing

Segments 1 and 6 were selected for line scan analyses, because of better visible preservation of the ejecta layer during all processing. Therefore, 7 and 12 LA-ICP-MS lines scan were respectively conducted in segments 1 and 6 (Fig. 2c and d). Each profile was between 8 and 25 mm long and the analytical sampling was done at 20 μm steps (Fig. 2c and d). Between 345 and 1223 values were thus obtained, including between 29 and 360 data in the gray calcareous marl and marl (uppermost Maastrichtian), between 63 and 144 data in the ejecta layer, and between 127 and 879 data in the blackish-gray boundary clay interval (lowermost Danian).

A 193 nm wavelength COMPex 102 ArF excimer laser ablation system (Lambda Physik, Göttingen, Germany) connected to an Element 2 sector field ICP-MS (Thermo Scientific, Bremen, Germany) was used for all LA-ICP-MS analyses at the GML of Utrecht University (The Netherlands). The data were subsequently processed following the procedure of Sosa-Montes de Oca et al. (2018a, 2018b). The LA-ICP-MS specifications as well as elemental ratios used in this paper are summarized in Table 1.

Concretely, for our samples and with the goal to measure elements like Ir, Pt and Pd a specific external standard (WPR-1) was used,

**Table 1**
Typical LA-ICP-MS settings for measurements on resin embedded samples.

| ICP-MS type | Thermo Scientific Element 2 |
|---|---|
| RF power | 1300 W |
| Plasma gas | Ar (16.00 l $min^{-1}$) |
| Auxiliary gas | Ar (0.85 l $min^{-1}$) |
| Carrier gas | Ar (0.67 l $min^{-1}$) and He (0.75 l $min^{-1}$) |
| Skimmer cone | Aluminum |
| Sampler cone | Nickel |
| Measurement frequency | ~2.5–3 Hz |
| Resolution | Low (M/ΔM = 400) |
| Isotopes* | $^{23}$Na, $^{24}$Mg, $^{25}$Mg, $^{26}$Mg, **$^{27}$Al**, $^{29}$Si, $^{31}$P, **$^{43}$Ca**, **$^{44}$Ca**, **$^{49}$Ti**, $^{51}$V, **$^{52}$Cr**, $^{55}$Mn, **$^{57}$Fe**, $^{59}$Co, **$^{60}$Ni**, **$^{65}$Cu**, **$^{66}$Zn**, **$^{75}$As**, $^{88}$Sr, $^{89}$Y, $^{90}$Zr, $^{97}$Mo, $^{98}$Mo, $^{103}$Rh, **$^{105}$Pd**, **$^{121}$Sb**, $^{137}$Ba, $^{140}$Ce, $^{185}$Re, **$^{193}$Ir**, $^{194}$Pt, **$^{195}$Pt**, **$^{208}$Pb**, $^{232}$Th, $^{238}$U |
| Laser type | COMPex 102 (ArF Excimer, Lambda Physik) |
| Wavelength | 193 nm |
| Fluence | 8 J $cm^{-2}$ |
| Spot size diameter | 120 μm |
| Repetition rate | 10 Hz |
| Scanning rate | 0.0275 mm $s^{-1}$ |

* Elements used in this paper.

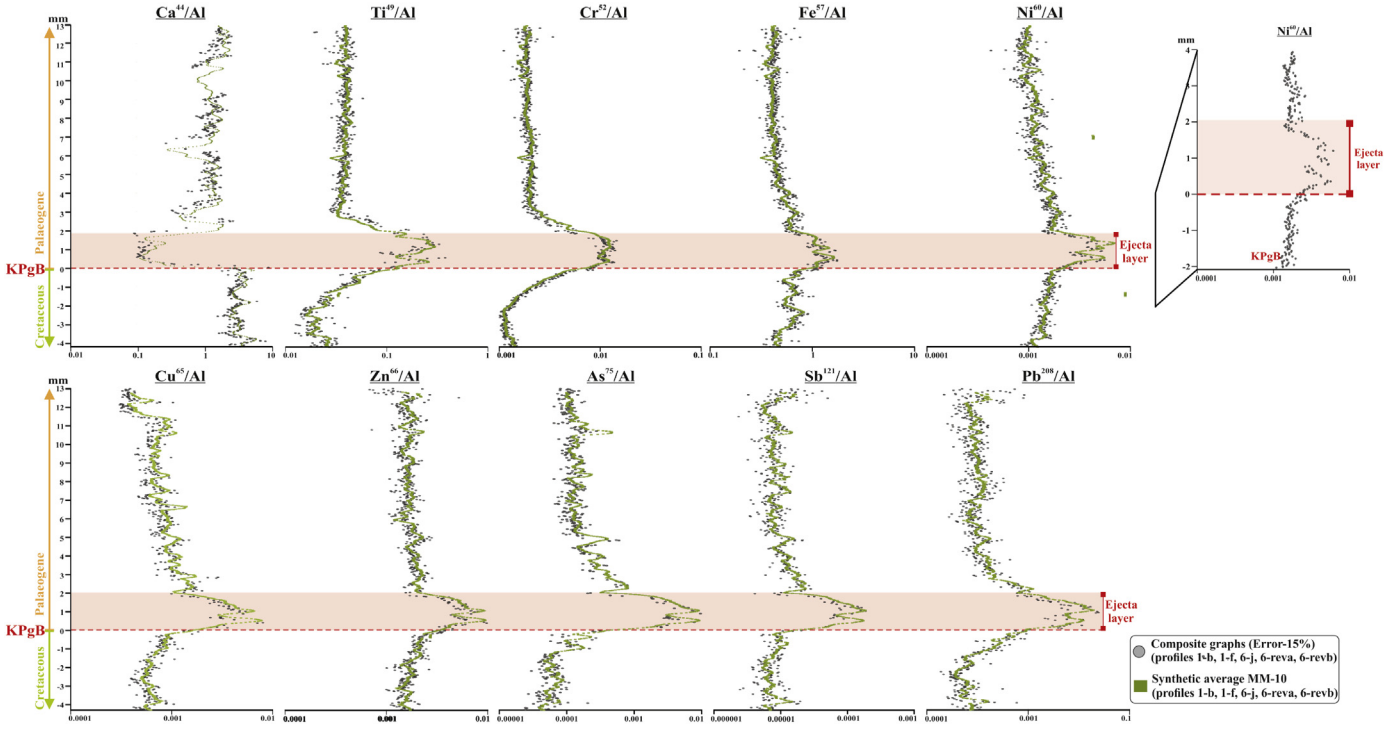


**Fig. 3.** Composite graphs and synthetic average (MM-10) from 1b, 1f, 6j, 6reva and 6revb profiles analyzed by LA-ICP-MS in a 17 mm-long interval across the KPgT in the Agost section. The elemental isotopic ratios measured were Ca/Al, Ti/Al, Cr/Al, Fe/Al, Ni/Al, Cu/Al, Zn/Al, As/Al, Sb/Al and Pb/Al and corresponding to the gray calcareous marl (uppermost Maastrichtian), the ejecta layer, and from the blackish-gray boundary clay (lowermost Danian). In the right corner there is a close up composite graph from the Ni/Al profile in 6 mm-long interval across the KPgT.

additionally to external standard (NIST SRM610) used for the other elements (see Sosa-Montes de Oca et al., 2018a, 2018b).

### 3.3. ICP-OES and ICP-MS analyses

Discrete samples from segments 1 and 6 were manual collected and analyzed by ICP-OES and ICP-MS. Specifically, nine samples were taken along 22 mm of segment 1, and six samples were taken along 17 mm of segment 6.

For the geochemical analysis, samples were crushed in an agate mortar and digested with $HNO_3$ + HF in order to obtain the sample solution. Trace element concentrations were determined using an ICP-Mass Spectrometry (NEXION 300D). Results were calibrated using blanks and international standards, with analytical precision better than ± 2% for 50 ppm elemental concentrations and ± 5% for 5 ppm elemental concentrations. The concentrations of major elements (Al, Ca, Fe, K and Mg) were measured in the same sample solutions using an ICP-Optical Emission Spectroscope (Perkin-Elmer Optima 8300) with an Rh anode X-ray tube. Blanks and international standards were used for quality control and the analytical precision was better than ± 2.8% and 1.9% for 50 ppm elemental concentrations of Al and Ca, respectively; better than ± 0.5% for 20 ppm elemental concentrations of Fe; better than ± 0.4% for 5 ppm elemental concentrations of K; and better than ± 1.5% for 2.5 ppm elemental concentrations of Mg. All the geochemical analyses were performed at the Center for Scientific Instrumentation (CIC), University of Granada, Spain.

Across the KPgB, a large shift in carbonate content occurs. For studying elemental variability without this carbonate dilution effect, Al-normalized concentrations or recalculation on a carbonate-free basis is usually applied (Calvert and Pedersen, 1993; De Lange et al., 1987; Morford and Emerson, 1999; Tribovillard et al., 2006; Van der Weijden, 2002). We have used the more straight-forward ratios versus Al. Those reported in this paper are Ca/Al, Cr/Al, Fe/Al, Ni/Al, Cu/Al, and Zn/Al.

### 3.4. High-Resolution Scanning Electron Microscopy (HRSEM)

Morphology and compositional information was also obtained from High-Resolution Scanning Field Scanning Electron Microscope (HRSEM) (AURIGA from Carl Zeiss SMT, CIC, University of Granada, Spain) equipped with an Oxford energy-dispersive X-ray spectrometer (EDX), used to quantitatively analyze the elements present in the selected areas.

The analysis by HRSEM focused on the transition between the gray calcareous marlstones from the uppermost Maastrichtian and the ejecta layer from the lowermost Danian.

## 4. Results

### 4.1. Analytical results of LA-ICP-MS

After LA-ICP-MS measurements, the data for all profiles were processed, that is 7 profiles for segment 1 (see Appendix B of the supplementary material), with path-lengths between 8 and 25 mm long, and 12 profiles for segment 6 (see Appendix C and Appendix D of the supplementary material), with lengths between 13 and 18 mm long. The profiles where the ejecta layer is unaffected by cracks were selected (i.e., profiles 1b and 1f for segment 1; and profiles 6j, 6reva and 6revb for segment 6). Cracks may have pre-existed and were augmented during the embedding procedure. Analytically, cracks lead to variability in the elemental ratios, due to edge effects of the abrasion surface, and are not homogeneous for all elements. Furthermore, it is important to take into account, that the remaining variability inside the ejecta layer is possibly attributable to the presence of different minerals typical of the ejecta layer (such as spherules or pyrite).

The final profiles, with the mean values of the 5 profiles selected (1b, 1f, 6j, 6reva, 6revb), resulted scatter and with several anomalous points. To clean these profiles, first values associated with major cracks were deleted. Subsequently, the data were subjected to statistical

treatment.

Different statistical treatments were done:

i) Firstly, a synthetic average was determined for the 5 profiles selected (1b, 1f, 6j, 6reva, 6revb) (Fig. 3). The synthetic average of the 5 profiles is the mean between the synthetic averages of each profile individually. Thus, the synthetic average throughout one full profile is mean value between those profiles whose absolute value of the subtraction between them is lower. For example; for the synthetic average of 1b-profile, is necessary to calculate, for each individual point along all profile, the absolute value of the subtraction between $|1b\text{-}1f|$, $|1b\text{-}6i|$, $|1b\text{-}6reva|$ and $|1b\text{-}6revb|$, if minor value between them is $|1b\text{-}1f|$, then for this point, the synthetic average is the mean value between the profile b and f. The same calculation is repeated along the full profile b (see Fig. 3).
ii) Secondly, composite graphs were made from the 5 selected profiles (Fig. 3). For the composite graphs, those values of the synthetic average of each profile, which present an error greater than 15%, in relation to the mean value of the 5 synthetic average profiles, were removed. The mean of the error values of 5 profiles formed composite graphs for a studied interval ≈17 mm long (Fig. 3) or for a studied interval ≈6 mm long (Fig. 3).

Neither the slight difference in the ejecta layer thickness among the different profiles not the anomalous values in the profiles were not taken into consideration since all of them were corrected following the aforementioned statistic treatment (the synthetic average and composite graphs).

Geochemical ratios Ca/Al, Ti/Al, Cr/Al, Fe/Al, Ni/Al, Cu/Al, Zn/Al, As/Al, Sb/Al and Pb/Al measured by LA-ICP-MS are given in Appendix A of the supplementary material. Furthermore, composite graphs for each element are represented for an interval of ≈17 mm long (831 data in total) (Fig. 3) and of ~6 mm long (295 data in total) (Fig. 3), including uppermost Maastrichtian gray calcareous marl and marl, ejecta layer and blackish-brown boundary clay interval of lowermost Danian.

### 4.2. ICP-OES and ICP-MS data

Geochemical data and profiles on discrete samples from segments 1 and 6 analyzed by ICP-OES and ICP-MS (ICP-OES/MS) are presented in Table 2 and Fig. 4.

For a selected set of discrete samples, the $CaCO_3^*$ content (calculated from Ca*2.5), Fe/Al, Cr/Al, Ni/Al, Cu/Al and Zn/Al ratios have been determined using ICP-OES/MS (Table 2; Fig. 4). These samples come from an ≈24 mm long interval, from segment 1 and 6. In all key intervals (a, b, c), between 1 and 4 samples were taken.

### 4.3. Comparing discrete-samples using ICP-OES and ICP-MS vs continuous-samples using LA-ICP-MS

The shared interval, covered by both discrete sampling/ICP-OES/MS and by continuous/LA-ICP-MS analyses, is 17.54 mm, including 4.75 mm of uppermost Maastrichtian gray calcareous marl and marl, 2.02 mm of the ejecta layer, and 10.77 mm of blackish-gray boundary clay interval from the lowermost Danian (Fig. 4).

For this interval, maximum values of ≈50% for $CaCO_3^*$ and ≈10 for Ca/Al ratio are registered in both, the gray calcareous marl from the uppermost Maastrichtian and the boundary clay interval from the lowermost Danian, while the ejecta layer is characterized by minimum values for $CaCO_3^*$ (between 10 and 20%) and Ca/Al ratio (0.09).

In contrast, significant increases in Fe/Al, Cr/Al, Ni/Al, Cu/Al and Zn/Al ratios are exclusively observed within the ejecta layer (Fig. 4), while in all profiles similar values are observed for the uppermost Maastrichtian sediments and for the lowermost Danian boundary clay interval (Fig. 4).

Within just a 6 mm interval (Fig. 5), the data obtained by LA-ICP-MS of 1f profile from segment 1 and by ICP-OES/MS from segment 1 can be compared (Fig. 5). The difference in analytical resolution is striking, being 0.09 mm and ~1 mm respectively. This represents, for the ~2.02 mm-thick ejecta layer, a much larger amount of analytical data by LA-ICP-MS using 20 μm increments than by discrete sampling using ICP-OES/MS (99 data versus 1–2 data). Accordingly, for this ejecta layer a single peak is observed in ICP-OES/MS analyses, whereas a range of constant values is obtained with LA-ICP-MS (Fig. 5).

## 5. Discussion

### 5.1. Geochemical anomalies across the ejecta layer

The conducted high-resolution analysis (continuous μm-scale) in the KPgB transition at the Agost section focused on elements such as Cr, Fe,

**Table 2**
Table with the elemental content (major) and elemental ratios, measured by ICP-OES and ICP-MS across a 20 mm-long interval (from −5 mm to 15 mm) from the sample 6 and a 22 mm-interval (from −2 mm to 20 mm) from the sample 1 in the KPgB at the Agost section, including the gray calcareous marlstones and malstones from the uppermost Maastrichtian, the ejecta layer (red color) and the boundary clay layer from the lowermost Danian. Al, Ca, CaO, $CaCO_3^*$, concentrations (%); Ca/Al and Fe/Al ratios; Cr/Al, Cu/Al, Ni/Al, and Zn/Al ratios ($\times 10^{-4}$).

| Samples Agost | | Distance KPgB (mm) | | Mayor elements (%) | | | | | Geochemical proxies (%/%) | | Geochemical proxies ($*10^{-4}$) | | | |
|---|---|---|---|---|---|---|---|---|---|---|---|---|---|---|
| | | | | Al | Ca | CaO | $CaCO_3^{(*)}$ | Fe | Fe/Al | Ca/Al | Cr/Al | Cu/Al | Ni/Al | Zn/Al |
| Segment-1 | Ag-1.9 | (+20) | 20 | 6.08 | 11.86 | 16.60 | 29.65 | 2.48 | 0.41 | 1.95 | 15.64 | 4.61 | 10.49 | 11.64 |
| | Ag-1.8 | (+15) | 15 | 6.33 | 11.32 | 15.85 | 28.30 | 2.53 | 0.40 | 1.79 | 16.02 | 4.73 | 10.63 | 12.39 |
| | Ag-1.7 | (+10) | 10 | 6.93 | 11.28 | 15.79 | 28.20 | 2.68 | 0.39 | 1.63 | 15.00 | 5.06 | 10.35 | 11.23 |
| | Ag-1.6 | (+5) | 5 | 7.31 | 9.35 | 13.08 | 23.37 | 3.09 | 0.42 | 1.28 | 18.35 | 6.57 | 11.59 | 12.28 |
| | Ag-1.5 | (1, 2) | 1.5 | 6.54 | 6.91 | 9.68 | 17.28 | 4.79 | 0.73 | 1.06 | 72.97 | 16.55 | 21.14 | 24.58 |
| | Ag-1.4 | (0, 1) | 0.5 | 5.47 | 11.12 | 15.57 | 27.80 | 4.37 | 0.80 | 2.03 | 56.29 | 12.21 | 18.94 | 20.58 |
| | Ag-1.3 | (−1, 0) | −0.5 | 4.63 | 13.92 | 19.49 | 34.80 | 3.62 | 0.78 | 3.01 | 12.02 | 5.72 | 13.99 | 12.95 |
| | Ag-1.2 | (−2, −1) | −1.5 | 4.35 | 15.36 | 21.50 | 38.40 | 3.29 | 0.76 | 3.53 | 10.01 | 6.13 | 13.34 | 12.79 |
| | Ag-1.1 | (−2, −1) | −2.0 | 3.78 | 18.94 | 26.52 | 47.35 | 2.22 | 0.59 | 5.01 | 9.95 | 7.34 | 11.81 | 13.88 |
| Segment-6 | Ag-6.6 | (+15) | 15 | 4.95 | 16.53 | 23.14 | 41.33 | 2.01 | 0.41 | 3.34 | 15.14 | 4.32 | 8.57 | 11.18 |
| | Ag-6.5 | (+10) | 10 | 5.88 | 14.00 | 19.60 | 35.00 | 2.38 | 0.41 | 2.38 | 15.12 | 4.15 | 8.59 | 11.47 |
| | Ag-6.4 | (+5) | 5 | 6.56 | 9.06 | 12.68 | 22.65 | 2.84 | 0.43 | 1.38 | 19.41 | 5.81 | 10.65 | 12.28 |
| | Ag-6.3 | (0, 2) | 1 | 7.50 | 2.20 | 3.08 | 5.49 | 6.65 | 0.89 | 0.29 | 91.29 | 25.26 | 27.89 | 36.98 |
| | Ag-6.2 | (−1) | −1.0 | 4.70 | 15.21 | 21.29 | 38.02 | 3.22 | 0.68 | 3.23 | 25.96 | 8.68 | 16.06 | 14.67 |
| | Ag-6.1 | (−5, −2) | −3.5 | 4.85 | 16.02 | 22.43 | 40.05 | 2.61 | 0.54 | 3.30 | 15.25 | 5.89 | 12.73 | 13.37 |

(*) Calculated from Ca*2.5.

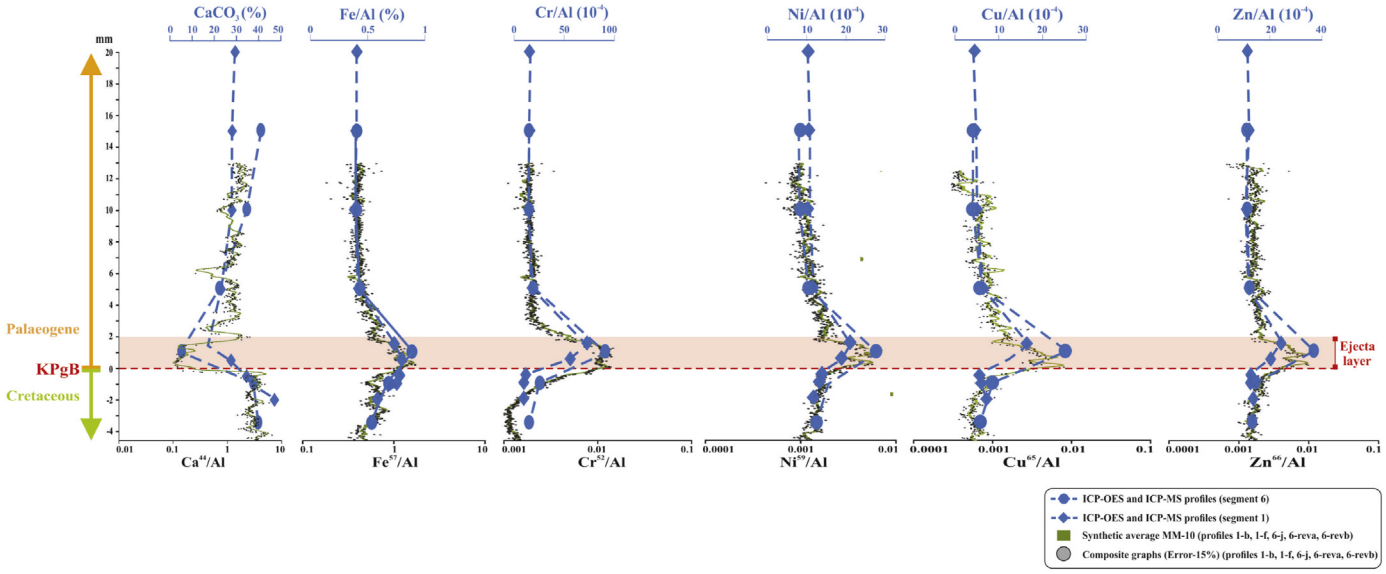


**Fig. 4.** Comparison of % $CaCO_3$*, Cr/Al, Ni/Al, Cu/Al, Zn/Al ($10^{-4}$) and Fe/Al ratio analyzed by ICP-OES and ICP-MS vs Ca/Al, Cr/Al, Fe/Al, Ni/Al, Cu/Al and Zn/Al ratios analyzed by LA-ICP-MS, in a 15.57 mm shared interval, including the gray calcareous marls (uppermost Maastrichtian), the ejecta layer, and the boundary clay layer (lowermost Danian).

Ni, Cu, and Zn. These are related with anoxic depositional conditions (Calvert and Pedersen, 1993; Tribovillard et al., 2006). The study revealed constant high concentrations in the selected elements linked exclusively to the ejecta layer. This fact supports similar oxygen conditions prior to and after the KPgB, and anoxic conditions restricted only to the brief episode of the ejecta layer deposition, estimated to be of the order of days to months at most (Artemieva and Morgan, 2009).

Lowery et al. (2018) have recently shown that the recovery of productivity in the Chicxulub structure is faster than in many other sites. They find that proximity to the impact was not a factor on recovery in marine ecosystems but linked it with the recovery of environmental conditions (e.g. oxygenation conditions).

Here we demonstrate that at the Agost distal section, the recovery of the oxygenation conditions may have been geologically instantaneous (in the range of days). This is also supported by the rapid recovery of the macrobenthic tracemaker community based on the presence of Fe-oxide spherules in the infilling of Thalassinoides traces in the Agost section (Rodríguez-Tovar, 2005) and the bioturbational disturbance of the 2–3-mm-thick K/Pg red boundary layer at the deeper Caravaca section (Rodríguez-Tovar and Uchman, 2008).

Hence, the rapid re-establishment of the oxic conditions at the distal sections of KPgB, led to a quick recovery of the opportunistic organisms of the macrobenthic tracemarker community. This quick recovery of biological activity also led to the mixture of the infilling material of trace fossils, essentially as a result to the unconsolidated character of the sediment (Sosa-Montes de Oca et al., 2016).

### 5.2. *Comparing analytical continuously profiles obtained by LA-ICP-MS with HRSEM*

Comparing our continuous profiles obtained by LA-ICP-MS vs HRSEM analyses for elements such as Ca and Ti, within segment 6 (reva and revb profiles) (Fig. 6) also illustrates how the decrease of the Ca/Al ratio and the increase of the Ti/Al ratio are mainly associated with the ejecta layer, maintaining relatively constant values in the entire ejecta layer. For the Ca/Al profile (Fig. 6), minor decrease peaks are observed, mainly associated with the presence of spherules. Specifically, most of the spherules in the Agost distal section have a composition of Fe-oxides (goethite) or K-feldspar spherules (Martínez-Ruiz et al., 1997), thus tending to result in a slight decrease in our Ca/Al profiles (6reva and 6revb) (see Fig. 7).

In addition, at the top the ejecta layer, a rapid increase of Ca/Al

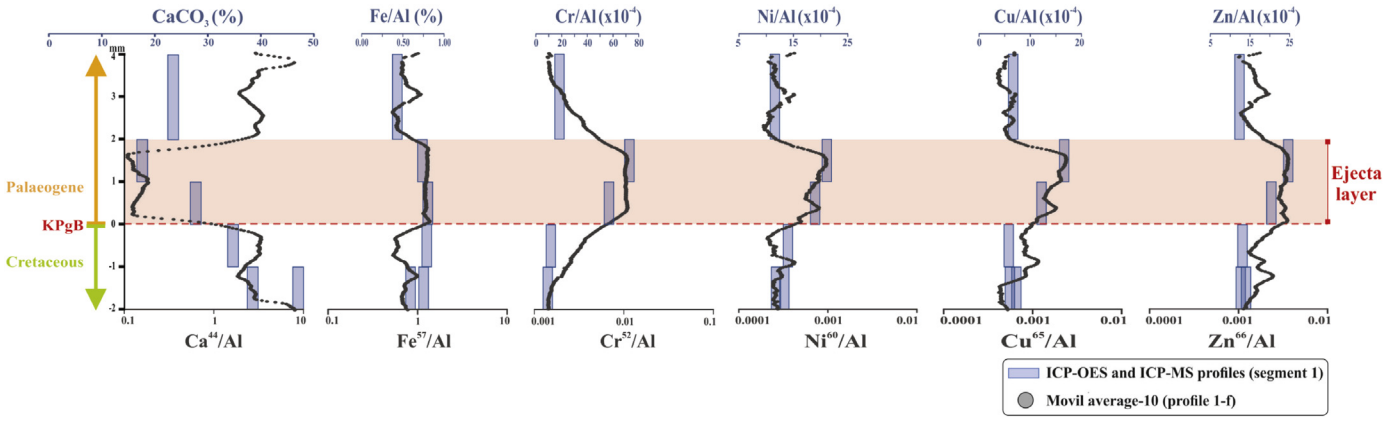


**Fig. 5.** Comparison of % $CaCO_3$*, Cr/Al, Ni/Al, Cu/Al, Zn/Al ($10^{-4}$) and Fe/Al ratio analyzed by ICP-OES and ICP-MS from the segment 1 vs the same ratios from the segment 1, profile f but analyzed by LA-ICP-MS, in a 6 mm interval, including the gray calcareous marlstones (uppermost Maastrichtian) and the ejecta layer and the boundary clay layer (lowermost Danian).

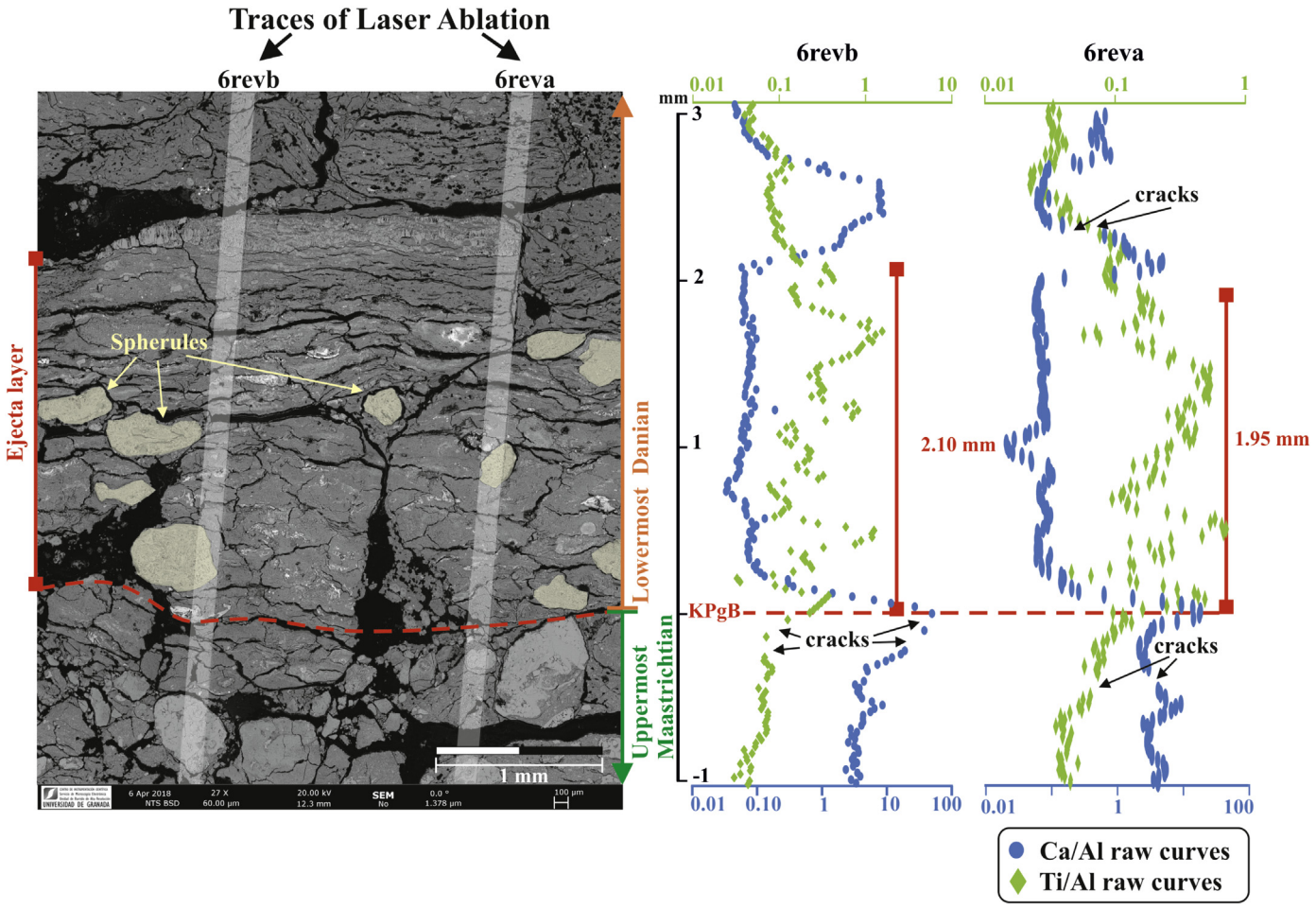


**Fig. 6.** Comparison between LA-ICP-MS traces (Ca/Al and Ti/Al ratios) and secondary electron images made by High-Resolution Scanning Electron Microscopy (HRSEM). In the photo are the traces of LA-ICP-MS (Trace 6reva and 6revb). The red dash line shows the KPgB. At the ejecta layer from the lowermost Danian, numerous spherules are observed (in yellow). Ca/Al profiles are in blue color while Ti/Al profiles are in green color. (For interpretation of the references to color in this figure legend, the reader is referred to the web version of this article.)

level is observed. However, for both segments this is due to the presence of a vein of diagenetic calcite (see Fig. 6 and Fig. 7). In fact, the total reestablishment of the Ca/Al ratio, and thus the carbonate content, occurred at the end of the boundary clay layer. From the ejecta layer upward, there is a gradual increase in the carbonate content to reach similar values to those in the Late Cretaceous (Ortega-Huertas et al., 2002; Smit, 1990, 1999).

In the case of the Ti/Al profiles (6reva and 6revb) (Fig. 6), some minor decrease/increase peaks are observed. These variations are associated to edge effects of the abrasion surface of the laser beam. Taking these potential deviations into account, we may consider the Ti/Al ratio to be rather constant across the ejecta layer.

Another interesting point to take into account, at this μm scale resolution, is the shape of the major peak associated with the ejecta layer in all elemental profiles (Figs. 3 and 5). The meteorite impact at the KPgB, implied an instantaneous contribution of a number of chemical markers (Kyte, 1998, 2002). However, the shape in which the increase/decrease appears starting a few mm below the ejecta layer is different for each element. Whereas a sharp decrease/indecrease is observed in the case of Ca, Fe, Ni, Cu, Zn, Pb, As and Sb profiles, a gradual increase is clearly observed in profiles for Ti and Cr (Figs. 3 and 5).

Titaniun is a rather immobile element thus the Ti/Al profile in Fig. 3 represents an unmobilized feature. Similarly, Cr, thought to be predominantly in a Cr-spinel mineral at the KPgB, thus largely refractory too, displays the same shape as Ti. Thus, any affect by postdepositional mobilisation can be excluded for these two elements. Consequently, the early onset of an increasing Ti and Cr flux immediately prior to the impact (≈100 yrs, according to the sedimentation rate of 2.05 cm $kyr^{-1}$ estimated for the uppermost Maastrichtian sediments), must be a primary signal. In contrast to the gradual onset observed for Cr, Ti, that for Ca is exclusively linked at the boundary and its increment is abrupt (Fig. 3).

Accordingly, this gradual onset for Cr, Ti, cannot be attributed to impact-related or sampling-related sediment mixing. Nor can it be related to any other form of physical mixing such as bioturbation, which has been previously tested in several KPgB sediments sections (Alegret et al., 2015; Kędzierski et al., 2011; Rodríguez-Tovar et al., 2010; Sosa-Montes de Oca et al., 2016). In the case that we had sediment mixing or bioturbation, all sedimentary components, and in particular $CaCO_3$* (here represented as Ca/Al), should demonstrate the same feature.

The gradually increasing flux observed for Ti and Cr profiles could only be related with a primary signal and with only 2 phenomena: a gradual onset of meteorite impacts (e.g. Jolley et al., 2010) or volcanic eruptions (e.g.; Renne et al., 2015; Schoene et al., 2015, 2019). However, based on our data, only for that one section, we cannot decide for any hypothesis, but can state that there was an external source for the explaining of these anomalies. Thus, further similar continuous high resolution studies (micro scale) are needed to corroborate if these anomalies are global or local.

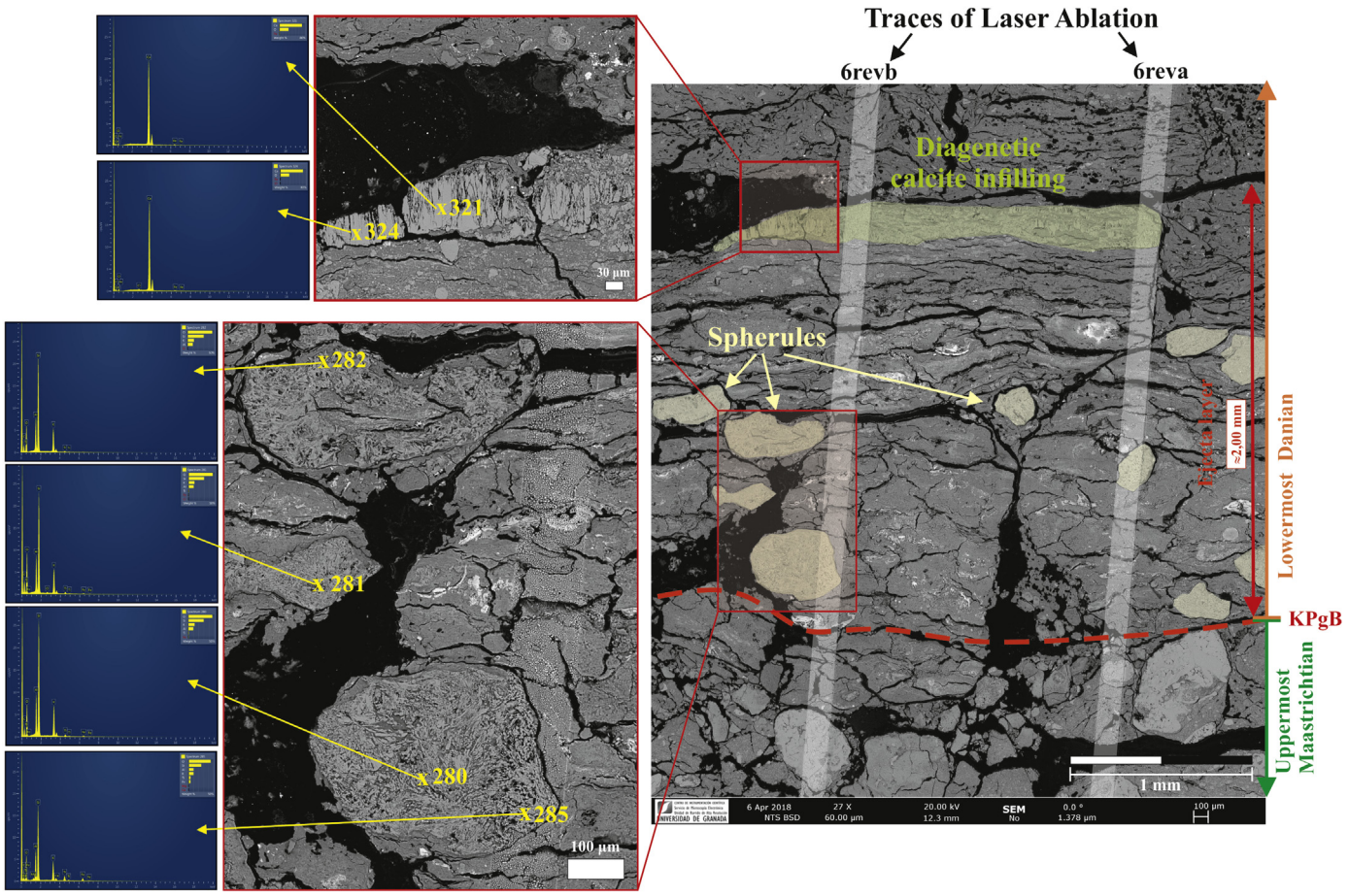


**Fig. 7.** Secondary electron image of segment 6 made by High-Resolution Scanning Electron Microscopy (HRSEM). Analyses of two selected areas were made by EDX. The spherules are marked in yellow whereas the diagenetic calcite is marked in green. (For interpretation of the references to color in this figure legend, the reader is referred to the web version of this article.)

### *5.3. High-resolution tentative profile of iridium and other PGE obtained by LA-ICP-MS*

Iridium has been traditionally analyzed by instrumental (INAA) and radiochemical (RNAA) neutron activation analysis (e.g. Alvarez et al., 1980, 1990; Smit and Hertogen, 1980), nickel sulfide fire assay (NiS) pre-concentration techniques and/or isotope dilution (ID) in combination with inductively coupled plasma-mass spectrometry (ICP-MS) (e.g. Claeys et al., 2002; Esmeray-Senlet et al., 2017; Goderis et al., 2013). Here, a constant high concentration ratios of iridium was observed using the high-resolution LA-ICP-MS methodology (Sosa-Montes de Oca et al., 2018a, 2018b) and a specific external standard as WPR-1 (Fig. 8).

Thus, from the 5 profiles initially chosen, we selected those where the specific external standard was used, (only 1f profile for segment 1; and 6reva and 6revb profiles for segment 6). As a result, in the iridium profile, a constant pattern with low scatter is observed in the ejecta layer (Fig. 8), despite the low concentration and the isobaric interference that this element could suffer. Elevated Ir/Al ratios can be detected and linked exclusively with the ejecta layer (Fig. 8). Nevertheless, future analytical developments may allow for better precision and detection and thus a more advanced interpretation of Ir data.

As the results from LA-ICP-MS analyses of Pt and Pd are close to the detection limit, it is not possible to detect a significant increase of the Pt/Al and Pd/Al ratios within the ejecta layer (Appendix E of supplementary material). Thus future developments of more accurate analysis including appropriate external standard would be required to improve the analytical quality for these elements.

Notwithstanding, abrupt enhanced levels of iridium linked only with the ejecta layer, which mainly is related with atmospheric projection estimated in the order of days to months at most (Artemieva and Morgan, 2009). Also support the idea of the quick recovery of oxic conditions and productivity after this event (e.g., Alegret et al., 2012; Alegret and Thomas, 2009; Birch et al., 2016; Esmeray-Senlet et al., 2015; Schueth et al., 2015; Sepúlveda et al., 2009; Sosa-Montes de Oca et al., 2013, 2016, 2017). This is of special interest in the context of evolutionary and ecological dynamics (e.g., Hull, 2015).

This recovery time for the oxic conditions after KPg event, could be of special interest to know how the recovery of the current climate change could be (Pachauri et al., 2014).

In sum, thanks to the continuous high-resolution analyses performed here, it could be possible to reconstruct the main anomalies associated with the KPgB, at the onset, the event itself and finally at the recovery to pre-impact conditions. Thus, in the sediments from the uppermost Cretaceous, a gradual rise on the concentration of elements like Ti and Cr was observed started ≈100 yrs. previously to the event. During ejecta layer deposition an abrupt increase of elements such as Ti, Cr, Cu, Fe, Ni, Zn, Pb and Ir was related to the meteorite's own contribution (Kyte, 1998, 2002) whereas abrupt increase of As, Sb levels are associated with Fe,S/ox dynamics (Mizan et al., 2017). Finally, once the ejecta layer was deposited, similar concentrations of, Fe, Ni, Cu, Zn, As, Sb, Pb and Ir, to that in the uppermost Cretaceous were observed, thus leading one to interpret similar oxygen conditions prior to and after the KPgB, with anoxic environments restricted only to the brief episode of ejecta layer deposition, estimated in the order of days to months at most (Artemieva and Morgan, 2009).

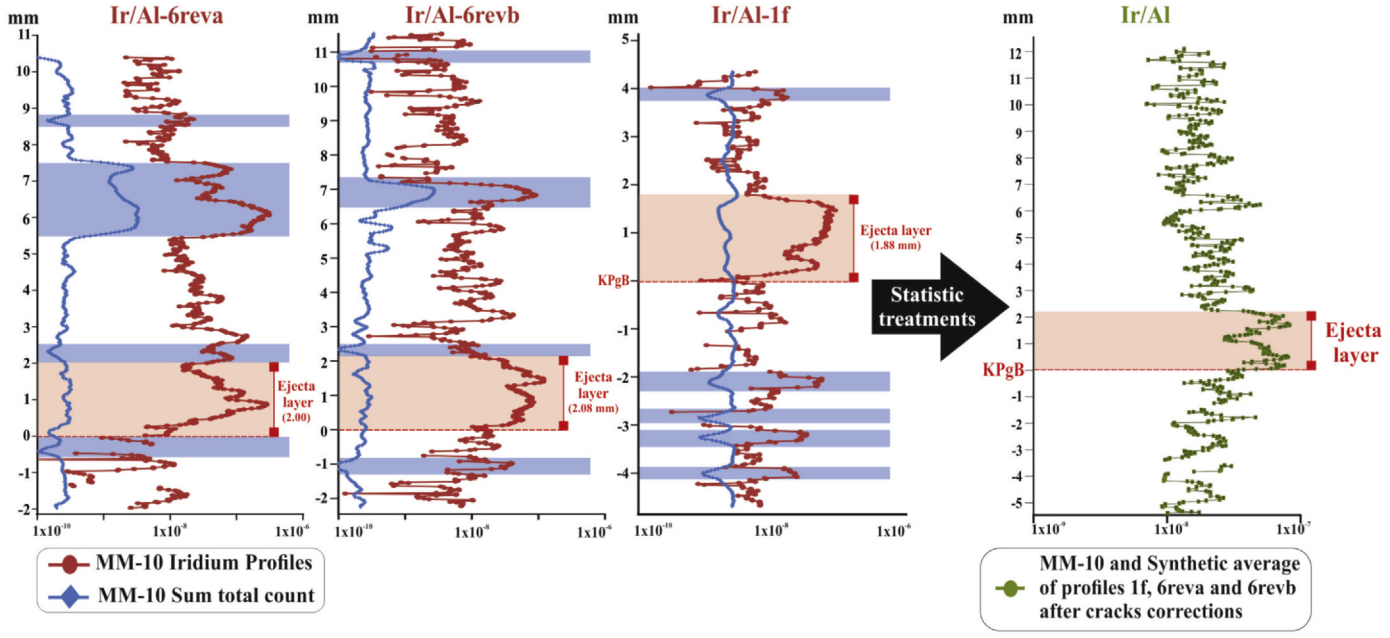


**Fig. 8.** Iridium profile measured by LA-ICP-MS in an ≈18 mm-long interval across the KPgT in the Agost section. In green color there is the synthetic average with 10 points moving average of 1f, 6reva and 6revb profiles for each element. In blue color there are the sum total counts from 1f, 6reva and 6revb profiles, with 10 points moving average, which are related with the cracks presented in each profile. In red color there are the Ir/Al ratios from 1f, 6reva and 6revb profiles with a 10 points moving average. (For interpretation of the references to color in this figure legend, the reader is referred to the web version of this article.)

## 6. Conclusions

High-resolution analyses performed in the distal section of Agost (Southeast Spain) by LA-ICP-MS in continuous measurements with 20 μm increments prior resin-embedded, provide evidence of an instantaneous reestablishment of the oxygen conditions after the impact event. The anoxic conditions are exclusively restricted to the ejecta layer deposition, which was near instantaneous (in the range of days). The rapid re-establishment of the oxygenation conditions, immediately after deposition of the ejecta layer, resulted in a quick recovery of the opportunistic organisms of the macrobenthic tracemarker community.

Furthermore, at this scales' resolution, an early onset of Ti and Cr, few millimeters below the ejecta layer, were reported for first time in the KPgB sediments. This is a primary signal, however due to the fact that this study has only been done at the Agost section, further studies are crucial to decide what the cause of the influx of these elements was.

LA-ICP-MS in continuous mode is a useful technique for detecting minor geochemical variations within the ejecta layer. These may relate to variability in mineralogical fragments, and may also elucidate the presence of an iridium anomaly.

Supplementary data to this article can be found online at https://doi.org/10.1016/j.chemgeo.2019.119431.

## Acknowledgments

We are grateful to Professor Donald Porcelli (Chemical Geology editor), and both reviewers, Dr. Armelle Riboulleau and one anonymous for their valuable comments and suggestions. This research was funded through Projects CGL2012-33281, CGL2012-32659, CGL2015-66835, and CGL2015-66830, Project RNM-05212 (Secretaría de Estado de I+D+I, Spain), Research Groups RNM-178 and RNM-179 (Junta de Andalucía), the Scientific Excellence Unit UCE-2016-05 (Universidad de Granada), and FEDER funds. The research of Sosa-Montes de Oca was supported by a pre-doctoral fellowship from the Spanish Ministry, MINECO. Furthermore, we acknowledge the access to the LA-ICP-MS facility at Geociences-Utrecht and in particular the skillful assistance by Helen de Waard during the LA-ICP-MS analysis. The ICP-MS, ICP-OES and HRSEM analyses were performed at the Centre for Scientific Instrumentation (CIC), University of Granada (Spain).

## References

Alegret, L., Thomas, E., 2009. Food supply to the seafloor in the Pacific Ocean after the Cretaceous/Paleogene boundary event. Mar. Micropaleontol. 73, 105–116. https://doi.org/10.1016/j.marmicro.2009.07.005.

Alegret, L., Thomas, E., Lohmann, K.C., 2012. End-Cretaceous marine mass extinction not caused by productivity collapse. Proc. Natl. Acad. Sci. U. S. A. 109, 728–732. https://doi.org/10.1073/pnas.1110601109.

Alegret, L., Rodríguez-Tovar, F.J., Uchman, A., 2015. How bioturbation obscured the Cretaceous-Palaeogene boundary record. Terra Nov 27, 225–230. https://doi.org/10.1111/ter.12151.

Alvarez, L.W., Alvarez, W., Asaro, F., Michel, H.V., 1980. Extraterrestrial cause for the Cretaceous-Tertiary extinction. Science (80-. ) 208, 1095–1108.

Alvarez, W., Asaro, F., Montanari, A., 1990. Iridium profile for 10 million years across the Cretaceous-Tertiary boundary at Gubbio (Italy). Science 250, 1700–1702.

Artemieva, N., Morgan, J., 2009. Modeling the formation of the K-Pg boundary layer. Icarus 201, 768–780. https://doi.org/10.1016/j.icarus.2009.01.021.

Artemieva, N., Morgan, J., 2017. Quantifying the release of climate-active gases by large meteorite impacts with a case study of Chicxulub. Geophys. Res. Lett. 44, 10,180–10,188. https://doi.org/10.1002/2017GL074879.

Birch, H.S., Coxall, H.K., Pearson, P.N., Kroon, D., Schmidt, D.N., 2016. Partial collapse of the marine carbon pump after the Cretaceous-Paleogene boundary. Geology 44, 287–290. https://doi.org/10.1130/G37581.1.

Calvert, S.E., Pedersen, T.F., 1993. Geochemistry of Recent oxic and anoxic marine sediments: implications for the geological record. Mar. Geol. 113, 67–88.

Claeys, P., Kiessling, W., Alvarez, W., 2002. Distribution of Chicxulub ejecta at the Cretaceous-Tertiary boundary. Geol. Soc. Am. Spec. Pap. 356, 55–68. https://doi.org/10.1130/0-8137-2356-6.55.

De Lange, G.J., Van der Sloot, H.A., Wijkstra, J., 1987. Implications of the diagenetic mobility of Ir for the interpretation of the anomaly at the K/T boundary. Geol. Soc. Spec. Publ. 31, 147–165.

Esmeray-Senlet, S., Wright, J.D., Olsson, R.K., Miller, K.G., Browning, J.V., Quan, T.M., 2015. The Cretaceous/Paleogene mass extinction. Paleoceanography 30, 718–738. https://doi.org/10.1002/2014PA002724.Received.

Esmeray-Senlet, S., Miller, K.G., Sherrell, R.M., Senlet, T., Vellekoop, J., Brinkhuis, H., 2017. Iridium profiles and delivery across the Cretaceous/Paleogene boundary. Earth Planet. Sci. Lett. 457, 117–126. https://doi.org/10.1016/j.epsl.2016.10.010.

Glass, B., Burns, C.A., 1987. Late Eocene crystal-bearing spherules — 2 layers or one — a reply. Meteoritics 23, 265–279.

Goderis, S., Tagle, R., Belza, J., Smit, J., Montanari, A., Vanhaecke, F., Erzinger, J., Claeys, P., 2013. Reevaluation of siderophile element abundances and ratios across the Cretaceous-Paleogene (K-Pg) boundary: implications for the nature of the projectile. Geochim. Cosmochim. Acta 120, 417–446. https://doi.org/10.1016/j.gca.2013.06.010.

Groot, J.J., de Jonge, R.B.G., Langereis, C.G., ten Kate, W.G.H.Z., Smit, J., 1989. Magnetostratigraphy of the Cretaceous-Tertiary boundary at Agost (Spain). Earth Planet. Sci. Lett. 94, 385–397. https://doi.org/10.1016/0012-821X(89)90155-6.

Hennekam, R., Jilbert, T., Mason, P.R.D., de Lange, G.J., Reichart, G.J., 2015. High-resolution line-scan analysis of resin-embedded sediments using laser ablation-inductively coupled plasma-mass spectrometry (LA-ICP-MS). Chem. Geol. 403, 42–51. https://doi.org/10.1016/j.chemgeo.2015.03.004.

Hull, P., 2015. Life in the aftermath of mass extinctions. Curr. Biol. 25, R941–R952. https://doi.org/10.1016/j.cub.2015.08.053.

Husson, D., Galbrun, B., Gardin, S., Thibault, N., 2014. Tempo and duration of short-term environmental perturbations across the Cretaceous-Paleogene boundary. Stratigraphy 11, 159–171.

Jilbert, T., de Lange, G.J., Reichart, G.J., 2008. Fluid displacive resin embedding of laminated sediments: preserving trace metals for high-resolution paleoclimate investigations. Limnol. Oceanogr. Methods 6, 16–22. https://doi.org/10.4319/lom.2008.6.16.

Jolley, D., Gilmour, I., Gurov, E., Kelley, S., Watson, J., 2010. Two large meteorite impacts at the Cretaceous-Paleogene boundary. Geology 38, 835–838. https://doi.org/10.1130/G31034.1.

Kędzierski, M., Rodríguez-Tovar, F.J., Uchman, A., 2011. Vertical displacement and taphonomic filtering of nannofossils by bioturbation in the Cretaceous-Palaeogene boundary section at Caravaca, SE Spain. Lethaia 44, 321–328. https://doi.org/10.1111/j.1502-3931.2010.00244.x.

Kring, D.A., 2007. The Chicxulub impact event and its environmental consequences at the Cretaceous-Tertiary boundary. Palaeogeogr. Palaeoclimatol. Palaeoecol. 255, 4–21. https://doi.org/10.1016/j.palaeo.2007.02.037.

Kyte, F.T., 1998. A meteorite from the Cretaceous/Tertiary boundary. Nature 396, 237–239.

Kyte, F.T., 2002. Tracers of the Extraterrestrial Component in Sediments and Inferences for Earth's Accretion History. Special Paper of the Geological Society of Americahttps://doi.org/10.1130/0-8137-2356-6.21.

Lowery, C.M., Bralower, T.J., Owens, J.D., Rodríguez-tovar, F.J., Jones, H., Smit, J., Gulick, S., Joanna, V., Green, S., Chenot, E., Whalen, M.T., Claeys, P., Farley, K., Sean, P., 2018. Rapid recovery of life at ground zero of the end-Cretaceous mass extinction. Nature. https://doi.org/10.1038/s41586-018-0163-6.

Martínez-Ruiz, F., Ortega-Huertas, M., Palomo, I., Acquafredda, P., 1997. Quench textures in altered spherules from the Cretaceous-Tertiary boundary layer at Agost and Caravaca, SE Spain. Sediment. Geol. 113, 137–147. https://doi.org/10.1016/S0037-0738(97)00057-2.

Mizan, S.A., Chatterjee, A., Ahmed, S., 2017. Arsenic enrichment in groundwater in southern flood plain of Ganga-Son interfluves. Arab. J. Geosci. 10, 0–10. https://doi.org/10.1007/s12517-017-2880-9.

Molina, E., Alegret, L., Arenillas, I., Arz, J.A., 2005. The Cretaceous/Paleogene boundary at the Agost section revisited: paleoenvironmental reconstruction and mass extinction pattern. J. Iber. Geol. 31, 135–148.

Morford, J.L., Emerson, S., 1999. The geochemistry of redox sensitive trace metals in sediments. Geochim. Cosmochim. Acta 63, 1735–1750. https://doi.org/10.1016/S0016-7037(99)00126-X.

Ortega-Huertas, M., Martínez-Ruiz, F., Palomo, I., Chamley, H., 2002. Review of the mineralogy ot the Cretaceous-Tertiary boundary clay: evidence supporting a major extraterrestrial catastrophic event. Clay Miner. 37, 395–411. https://doi.org/10.1180/0009855023730054.

Pachauri, R.K., Allen, M.R., Barros, V.R., Broome, J., Cramer, W., Christ, R., Church, J.A., Clarke, L., Dahe, Q., Dasgupta, P., 2014. Climate Change 2014: Synthesis Report, Climate Change 2014 — Synthesis Report. https://doi.org/10.1017/CBO9781107415324.

Renne, P.R., Deino, A.L., Hilgen, F.J., Kuiper, K.F., Mark, D.F., Mitchell, W.S., Morgan, L.E., Mundil, R., Smit, J., 2013. Time scales of critical events around the Cretaceous-Paleogene boundary. Science 339, 684–687. https://doi.org/10.1126/science.1230492.

Renne, P.R., Sprain, C.J., Richards, M.A., Self, S., Vanderkluysen, L., Pande, K., 2015. Possibly induced by impact. Science (80-. ) 350, 76–78. https://doi.org/10.1126/science.aac7549.

Rodríguez-Tovar, F.J., 2005. Fe-oxide spherules infilling Thalassinoides burrows at the Cretaceous-Paleogene (K-P) boundary: evidence of a near-contemporaneous macrobenthic colonization during the K-P event. Geology 33, 585–588. https://doi.org/10.1130/G21527.1.

Rodríguez-Tovar, F.J., Uchman, A., 2008. Bioturbational disturbance of the Cretaceous-Palaeogene (K-Pg) boundary layer: implications for the interpretation of the K-Pg boundary impact event. Geobios 41, 661–667. https://doi.org/10.1016/j.geobios.2008.01.003.

Rodríguez-Tovar, F.J., Martínez-Ruiz, F., Bernasconi, S.M., 2006. Use of high-resolution ichnological and stable isotope data for assessing completeness of a K-P boundary section, Agost, Spain. Palaeogeogr. Palaeoclimatol. Palaeoecol. 237, 137–146. https://doi.org/10.1016/j.palaeo.2005.11.019.

Rodríguez-Tovar, F.J., Uchman, A., Molina, E., Monechi, S., 2010. Bioturbational redistribution of Danian calcareous nannofossils in the uppermost Maastrichtian across the K-Pg boundary at Bidart, SW France. Geobios 43, 569–579. https://doi.org/10.1016/j.geobios.2010.03.002.

Schoene, B., Samperton, K.M., Eddy, M.P., Keller, G., Adatte, T., Bowring, S.A., Khadri, S.F.R., Gertsch, B., 2015. U-Pb geochronology of the Deccan Traps and relation to the end-Cretaceous mass extinction. Science (80-. ) 347, 182–184. https://doi.org/10.1126/science.aaa0118.

Schoene, B., Eddy, M.P., Samperton, K.M., Keller, C.B., Keller, G., Adatte, T., Khadri, S.F.R., 2019. U-Pb constraints on pulsed eruption of the Deccan Traps across the end-Cretaceous mass extinction. Science (80-. ) 363, 862–866. https://doi.org/10.1126/science.aau2422.

Schueth, J.D., Bralower, T.J., Jiang, S., Patzkowsky, M.E., 2015. The role of regional survivor incumbency in the evolutionary recovery of calcareous nannoplankton from the Cretaceous/Paleogene (K/Pg) mass extinction. Paleobiology 41, 661–679. https://doi.org/10.1017/pab.2015.28.

Schulte, P., Alegret, L., Arenillas, I., Arz, J.A., Barton, P., Paul, R., Bralower, T.J., Christeson, G.L., Claeys, P., Cockell, C.S., Collins, G.S., Deutsch, A., Goldin, T.J., Goto, K., José, M., Grieve, R.A.F., Gulick, S.P.S., Johnson, K.R., Koeberl, C., Kring, D.A., Macleod, K.G., Matsui, T., Melosh, J., Montanari, A., Morgan, J.V., Neal, C.R., Douglas, J., Norris, R.D., Pierazzo, E., Ravizza, G., Rebolledo-vieyra, M., Reimold, W.U., Robin, E., Salge, T., Speijer, R.P., Sweet, A.R., Vajda, V., Whalen, M.T., Willumsen, P.S., 2010a. Supporting online material for the Chicxulub asteroid impact and mass extinction at the Cretaceous-Paleogene boundary. Science (80-. ). 327, 1214–1218. https://doi.org/10.1126/science.1177265.

Schulte, P., Alegret, L., Arenillas, I., Arz, J.A., Barton, P.J., Bown, P.R., Bralower, T.J., Christeson, G.L., Claeys, P., Cockell, C.S., Collins, G.S., Deutsch, A., Goldin, T.J., Goto, K., Grajales-Nishimura, J.M., Grieve, R.A.F., Gulick, S.P.S., Johnson, K.R., Kiessling, W., Koeberl, C., Kring, D.A., MacLeod, K.G., Matsui, T., Melosh, J., Montanari, A., Morgan, J.V., Neal, C.R., Nichols, D.J., Norris, R.D., Pierazzo, E., Ravizza, G., Rebolledo-Vieyra, M., Reimold, W.U., Robin, E., Salge, T., Speijer, R.P., Sweet, A.R., Urrutia-Fucugauchi, J., Vajda, V., Whalen, M.T., Willumsen, P.S., 2010b. The Chicxulub asteroid impact and mass extinction at the Cretaceous-Paleogene boundary. Science (80-. ) 327, 1214–1218. https://doi.org/10.1126/science.1177265.

Sepúlveda, J., Wendler, J.E., Summons, R.E., Hinrichs, K.-U., 2009. Rapid resurgence of marine productivity after the Cretaceous-Paleogene mass extinction. Science (80-. ) 326, 129–132. https://doi.org/10.1126/science.1176233.

Shukolyukov, A., Lugmair, G.W., 2004. Manganese-chromium isotope systematics of enstatite meteorites. Geochim. Cosmochim. Acta 68, 2875–2888. https://doi.org/10.1016/j.gca.2004.01.008.

Smit, J., 1990. Meteorite impact, extinctions and the Cretaceous-Tertiary boundary. Geol. en Mijnb. 69, 187–204.

Smit, J., 1999. The global stratigraphy of the Cretaceous-Tertiary boundary impact ejecta. Annu. Rev. Earth Planet. Sci. 27, 75–113.

Smit, J., Hertogen, J., 1980. An extraterrestrial event at the Cretaceous-Tertiary boundary. Nature 285, 198–200.

Smit, J., Klaver, G., 1981. Sanidine spherules at the Cretaceous-Tertiary boundary indicate a large impact event. Nature 292, 47–49.

Smit, J., Ten Kate, W.G.H.Z., 1982. Trace-element patterns at the Cretaceous-Tertiary boundary—consequences of a large impact. Cretac. Res. 3, 307–332.

Smith, A.G., Hurley, A.M., Briden, J.C., 1981. Phanerozoic Paleocontinental World Maps. CUP Archive.

Sosa-Montes de Oca, C., Martínez-Ruiz, F., Rodríguez-Tovar, F.J., 2013. Bottom-water conditions in a marine basin after the Cretaceous-Paleogene impact event: timing the recovery of oxygen levels and productivity. PLoS One 8, e82242. https://doi.org/10.1371/journal.pone.0082242.

Sosa-Montes de Oca, C., Rodríguez-Tovar, F.J., Martínez-Ruiz, F., 2016. Geochemical and isotopic characterization of trace fossil infillings: new insights on tracemaker activity after the K/Pg impact event. Cretac. Res. 57, 391–401. https://doi.org/10.1016/j.cretres.2015.03.003.

Sosa-Montes de Oca, C., Rodríguez-Tovar, F.J., Martínez-Ruiz, F., Monaco, P., 2017. Paleoenvironmental conditions across the Cretaceous–Paleogene transition at the Apennines sections (Italy): an integrated geochemical and ichnological approach. Cretac. Res. 71. https://doi.org/10.1016/j.cretres.2016.11.005.

Sosa-Montes de Oca, C., de Lange, G.J., Martínez-Ruiz, F., Rodríguez-Tovar, F.J., 2018a. Application of laser ablation-ICP-MS to determine high-resolution elemental profiles across the Cretaceous/Paleogene boundary at Agost (Spain). Palaeogeogr. Palaeoclimatol. Palaeoecol. 497, 128–138. https://doi.org/10.1016/j.palaeo.2018.02.012.

Sosa-Montes de Oca, C., de Lange, G.J., Martínez-Ruiz, F., Rodríguez-Tovar, F.J., 2018b. High-resolution data from Laser Ablation-ICP-MS and by ICP-OES analyses at the Cretaceous/Paleogene boundary section at Agost (SE Spain). Data Br 18, 1900–1906. https://doi.org/10.1016/j.dib.2018.04.118.

Thibault, N., Husson, D., 2016. Climatic fluctuations and sea-surface water circulation patterns at the end of the Cretaceous era: calcareous nannofossil evidence. Palaeogeogr. Palaeoclimatol. Palaeoecol. 441, 152–164. https://doi.org/10.1016/j.palaeo.2015.07.049.

Tribovillard, N., Algeo, T.J., Lyons, T., Riboulleau, A., 2006. Trace metals as paleoredox and paleoproductivity proxies: an update. Chem. Geol. 232, 12–32. https://doi.org/10.1016/j.chemgeo.2006.02.012.

Urrutia-Fucugauchi, J., Pérez-Cruz, L., 2016. Planetary sciences, geodynamics, impacts, mass extinctions, and evolution: developments and interconnections. Int. J. Geophys. 2016. https://doi.org/10.1155/2016/4703168.

Van der Weijden, C.H., 2002. Pitfalls of normalization of marine geochemical data using a common divisor. Mar. Geol. 184, 167–187.

Vellekoop, J., Woelders, L., van Helmond, N.A.G.M., Galeotti, S., Smit, J., Slomp, C.P., Brinkhuis, H., Claeys, P., Speijer, R.P., 2018. Shelf hypoxia in response to global warming after the Cretaceous-Paleogene boundary impact. Geology 46, 683–686. https://doi.org/10.1130/G45000.1.